Chapter 2
Carbothermal Reduction Synthesis: An Alternative Approach to Obtain Single-Crystalline Metal Oxide Nanostructures

M. O. Orlandi, P. H. Suman, R. A. Silva, and E. P. S. Arlindo

1 Introduction

In recent years, researchers in nanoscience and nanotechnology fields have focused on the development of new devices with optimized performance. Nanoscale materials, especially the single-crystalline ones, have attracted special attention as result of their size-dependent properties, which make them interesting candidates to be used as building blocks for the next generation of nanoelectronic/optoelectronic devices [1–3]. It is well known that material properties depend strongly on the processing parameters. Thereby, manufacturing materials in nanoscale with well-defined characteristics such as size, morphology, crystallinity, and chemical compositions have become a big challenge for technological applications [4–6].

Different approaches have been widely used to synthesize a variety of single-crystalline metal oxide nanostructures [7–9]. However, among these methods, the carbothermal reduction process emerges to be an interesting route, mainly due to its simplicity as well as its low cost and good quality of obtained materials [10]. This method is typically a chemical vapor deposition (CVD) process, in which a carbon source (e.g., carbon black, carbon nanotubes, graphite, etc.) is used as a reducing agent for increasing the vapor pressure of desired precursor. In this way, by controlling parameters like temperature, time, and the atmosphere of synthesis, single-crystalline nano- and microstructures can be grown in temperatures lower than the ones typically used in a conventional thermal evaporation route [10, 11].

M.O. Orlandi (✉) • P.H. Suman • R.A. Silva
Department of Physical-Chemistry, São Paulo State University, Araraquara, SP, 14800-900, Brazil
e-mail: orlandi@iq.unesp.br

E.P.S. Arlindo
Instituto de Ciências Exatas e da Terra, Federal University of Mato Grosso, Barra do Garças, MT, 78600-000, Brazil

E. Longo, F.A. La Porta (eds.), *Recent Advances in Complex Functional Materials*,
DOI 10.1007/978-3-319-53898-3_2

Based on the carbothermal reduction method, our group has synthesized several single-crystalline structures, such as tin oxide nanobelts in different oxidation states (SnO_2, SnO, and Sn_3O_4) and SnO micro-disks [10–12] as well as indium tin oxide (ITO) nanowires [13] and zinc oxide (ZnO) tetrapods [14]. These materials present high potential to be used in gas sensor application or transparent and conductive composite thin films [15, 16]. Other materials like carbides and phosphates have also been produced by using this method [17, 18].

Overall, controlling the synthesis of materials in nanoscale as well as understanding its growth mechanism is essential to produce materials in large scale. In this direction, the carbothermal reduction synthesis presents great potential to be used as a straightforward approach to producing single-crystalline nanomaterials for high-performance applications.

2 Principles of Carbothermal Reduction Process

Carbon is one of the most important chemical elements on Earth, and life is based on it. Besides, chemistry has a specific field focused on carbon study, which is the organic chemistry. So, carbon can be the main actor in many types of research, but it can also aim the research in materials science, working as a coadjutant actor. This is the base of carbothermal reduction method, in which the carbon is used to assist in the synthesis process.

The carbothermal reduction process is a versatile method, and it is based on the Ellingham diagram, as presented in Fig. 2.1. The Ellingham diagram is a plot of Gibbs free energy versus temperature and reactions appears like straight lines due to the following equation:

$$\Delta G = \Delta H – T\ \Delta S \tag{2.1}$$

in which ΔG is the change in the Gibbs free energy, ΔH is the enthalpy of formation, ΔS is the entropy variation, and T is the temperature. It is known that the free energy of an element decreases when it becomes an oxide, so the ΔG axis presents negative values in Fig. 2.1. The intercept is related to the enthalpy of formation, meaning the reaction is a spontaneous process. Besides, increasing the temperature the entropy of material decreases ($\Delta S < 0$), so straight lines with positive slope are expected.

Materials with small enthalpy of formation are at the top of the diagram, while materials with high enthalpy of formation are located at the bottom of it. So, it is expected that a material positioned at the bottom of Ellingham diagram can reduce a material located at the top of the diagram. However, instead of using one oxide to reduce another one, it is easier to use carbon. It is observed that the reaction $2C + O_2 \rightarrow 2CO$ has a negative slope, because 2 moles of solid carbon reacts with 1 mol of oxygen to generate 2 moles of CO, becoming more disordered.

In this way, it is possible to use carbon to reduce most of the oxides, since the temperature used is higher than the crossing point between the oxide reaction line and the abovementioned carbon reaction line. Using the Sn-O system as an example,

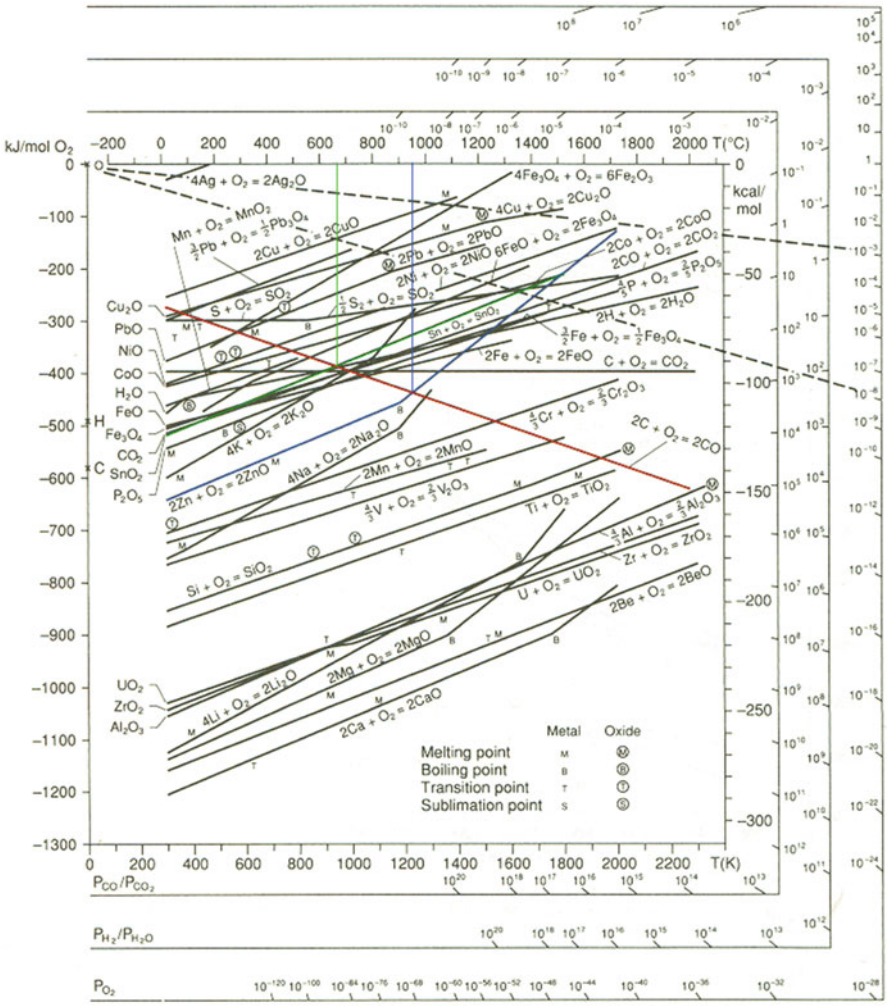

Fig. 2.1 The Ellingham diagram for several elements. The crossing points related to the formation of tin oxide and zinc oxide are indicated

Ellingham diagram shows that the crossing point between the $Sn + O_2 \rightarrow SnO_2$ and the $2C + O_2 \rightarrow 2CO$ reactions is around 680 °C, meaning that temperatures higher than it are enough to reduce the SnO_2. In fact, previous results showed that it is possible to synthesize SnO nanobelts at 900 °C [10]. Moreover, results also show that reducing an oxide increases its vapor pressure for most of oxides [19]. For instance, the SnO_2 vapor pressure at 1,250 °C is 3.6×10^{-5} Pa, while at the same temperature, the vapor pressure of SnO is 234.4 Pa [20], which is a large difference. In fact, results indicate that the vapor pressure of SnO_2 is enough to produce single-crystalline materials at temperatures higher than 1,350 °C [20, 21].

It means that the carbothermal reduction method enables to obtain nanocrystals of tin oxide at temperatures much lower than using direct evaporation, implying saving both costs and time of synthesis.

To perform the carbothermal reduction synthesis, in principle, any carbon source can be used, but the most common is the carbon black, although we also observed the growth of materials using graphite, carbon nanotubes, or even sugar. However, it is important to keep in mind that carbon black is a generic material used mainly as pigment, and there is variety of it, changing the particle size, morphology, and the conductivity. Up to now, there is no study about the efficiency of synthesis using different carbon sources.

Once the reaction between the carbon and the oxide is of fundamental importance for the synthesis process, the atmosphere must be carefully controlled, and oxygen leaks have to be avoided since it can react with carbon and jeopardize all this process.

Although studying the Ellingham diagram is a good starting point to have success in the synthesis of new complex materials, no rare a careful and dedicated work to find the best synthesis conditions is necessary.

Lieber et al. [22, 23] used the carbothermal reduction method to produce one-dimensional (1D) single-crystalline MgO nanorods with an average diameter of 20 nm. A detailed characterization showed rods grew in the [001] direction and were used to produce a composite in order to obtain high-temperature superconductors based on copper oxide. Guo et al. [24] reported beaded nanochains of silicon carbide obtained using carbothermal reduction method and its use to reinforce (0.5 wt%) epoxy-based composites. The mechanical tests showed an improvement of 32% in the tensile strength, which was attributed to the unique morphology obtained for the SiC material. Lead sulfide (PbS), which is an interesting material for nonlinear optical devices, was also prepared by carbothermal reduction process, resulting in PbS nanowires and nanobelts, both growing in the [110] direction.

Then, the carbothermal reduction process is an interesting method to use when it is desired to obtain single-crystalline 1D materials. Besides, it is very common that the grown materials are free of defects. Since 1D materials are the best ones to study electrical transport at the nanoscale, the carbothermal synthesis provides an excellent alternative to produce these complex materials.

Below we report a short introduction about the most common growth processes from the vapor phase, which are vapor-liquid-solid (VLS) and vapor-solid (VS), and after that we present the main results obtained by our group using the carbothermal reduction process, especially growing single-crystalline 1D materials.

3 Growth Mechanisms from Vapor Phase

Structures produced from vapor phase can follow basically two main growth mechanisms: vapor-liquid-solid (VLS) or vapor-solid (VS) [25, 26]. Other mechanisms were reported, but all of them are related in some way to the VS or VLS methods. A typical VLS growth mechanism starts with the adsorption of gaseous species in

a liquid metallic droplet. When the droplets become supersaturated by the vapor, the nucleation occurs followed by the growth of a solid from the droplet. The liquid droplet limits the lateral growth of material, which is important when 1D materials with controlled dimensions are desired [27, 28]. Besides, it is possible to have more control about the growth position by depositing catalyst droplets on specific sites on a substrate.

In contrast, in the VS method, 1D structures are generated only by changing the physical state of a starting material, usually by sublimation. It can occur in two different ways, called direct and indirect evaporation. In the indirect method, it is necessary for some chemical reaction to obtain the desired material. It occurs, for instance, when Mg vapor reacts with oxygen to provide MgO nanorods [23]. For the direct method, no chemical reaction is necessary, and it can occur to SiC, for example. In the VS process, no liquid particles are present during the growth of the structures, which allows to produce materials without any contamination by the metallic droplet. However, for the same reason, it is not possible to control accurately the structure dimensions and the position of the grown material.

4 Multiple Stoichiometries of Tin Oxide Nano- and Microstructures

Tin dioxide (SnO_2) is one of the most studied semiconducting materials, and due to its interesting physical and chemical properties, it has been used in several technological applications, such as sensors, fuel cells, and optical and electronic devices [29–32]. Pan, Dai, and Wang reported, for the first time, the synthesis of single-crystalline SnO_2 nanobelts by a simple thermal evaporation of oxide powders at high temperatures [33]. Since then, SnO_2 nanostructures including nanowires, nanotubes, and nanorods have been produced using several methods [34–36]. Moreover, other stoichiometries of tin oxide (e.g., SnO and Sn_3O_4) have also attracted a great attention in recent years [12, 15, 16].

Nano- and microstructures in different oxidation states of tin oxide (SnO_2, SnO, and Sn_3O_4) were synthesized by carbothermal reduction method from a mixture of SnO_2 powder (Sigma-Aldrich, 99.9% purity) and carbon black (Union Carbide, >99% purity) in the molar ratio of 1.5:1 (SnO_2:C). In a typical synthesis process, 1 g of this mixture was put into an alumina boat, which was introduced in the hot zone of a furnace tube with a sealing system at tube extremities, where both the temperature and the synthesis atmosphere are carefully controlled. The same starting material was used to perform synthesis runs at 1135 °C for 75 min but, using two different synthesis atmospheres, one inert and other oxidizing. To prepare SnO micro-disks and nanobelts, an inert synthesis atmosphere was established by a nitrogen gas flow of 80 sccm, whereas both SnO_2 and Sn_3O_4 nanobelts were synthesized in a controlled oxidizing synthesis atmosphere by using a nitrogen gas flow of 150 sccm and an oxygen gas flow of 0.5 sccm, which was introduced in the counterflow of

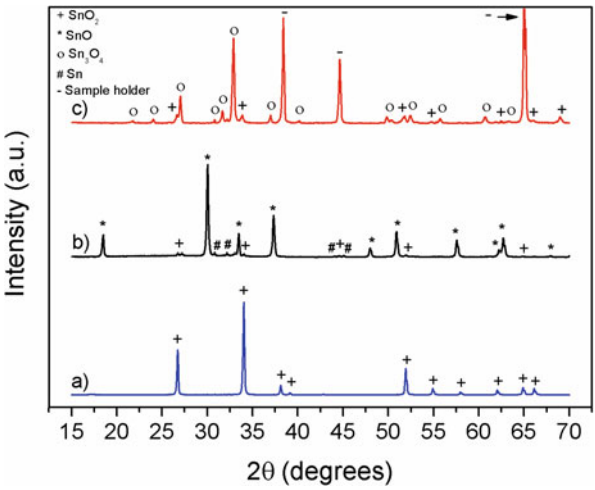

Fig. 2.2 XRD pattern of the (**a**) *white*, (**b**) *dark*, and (**c**) *yellow* woollike materials collected after the synthesis by carbothermal reduction method (Figure from Ref. [16] with permission from Elsevier)

nitrogen gas when the temperature reached 900 °C. Optimized parameters used to prepare all of these materials are described in detail in our previous reports [10, 12].

After both syntheses, woollike materials with different colors were collected in different regions from the inner walls of the alumina tube. In an inert synthesis atmosphere, a dark material was removed from the tube region where the temperature was about 350 °C. On the other hand, when an oxidizing synthesis atmosphere was established, both white and yellow materials were obtained where the temperature was about 500 °C and 700 °C, respectively.

Figure 2.2 shows the XRD spectra of the materials obtained after the synthesis by carbothermal reduction method. The XRD pattern of the white material (Fig. 2.2a) shows it is composed only by materials in the tetragonal structure of cassiterite SnO_2 phase (card JCPDS #41-1445), with evident preferential growth in the [101] direction. Figure 2.2b reveals that the dark material consists of three phases: SnO (card JCPDS #6-395), SnO_2 (card JCPDS #41-1445), and Sn° (card JCPDS #4-673). However, from the relative intensities of the peaks, it is clear that the SnO phase is the largest one, with minor contributions from SnO_2 and Sn° phases. It was found from Fig. 2.2c that the yellow material is constituted mainly of material's growth in the triclinic structure of the Sn_3O_4 (card JCPDS #16-0737) and a small amount in the tetragonal structure of cassiterite SnO_2 phase (card JCPDS #41-1445), as reported in the literature [2, 37]. The peaks marked with "-" ($2\theta = 38.4°$, 44.7° and 65.0°) are related to the aluminum sample holder. Based on the results obtained by XRD, it is notable that by controlling the synthesis atmosphere, structures in different stoichiometries of tin oxide can be produced.

Figure 2.3 shows the FE-SEM images of the SnO_2 materials collected after the synthesis. A low-magnification image (Fig. 2.3a) reveals that this material consists of 1D nanostructures with micrometers or even millimeters in length and rectangular cross-section, which are called nanobelts (Fig. 2.3b–c). Besides, it was observed that these structures present homogenous width along the length and have a smooth

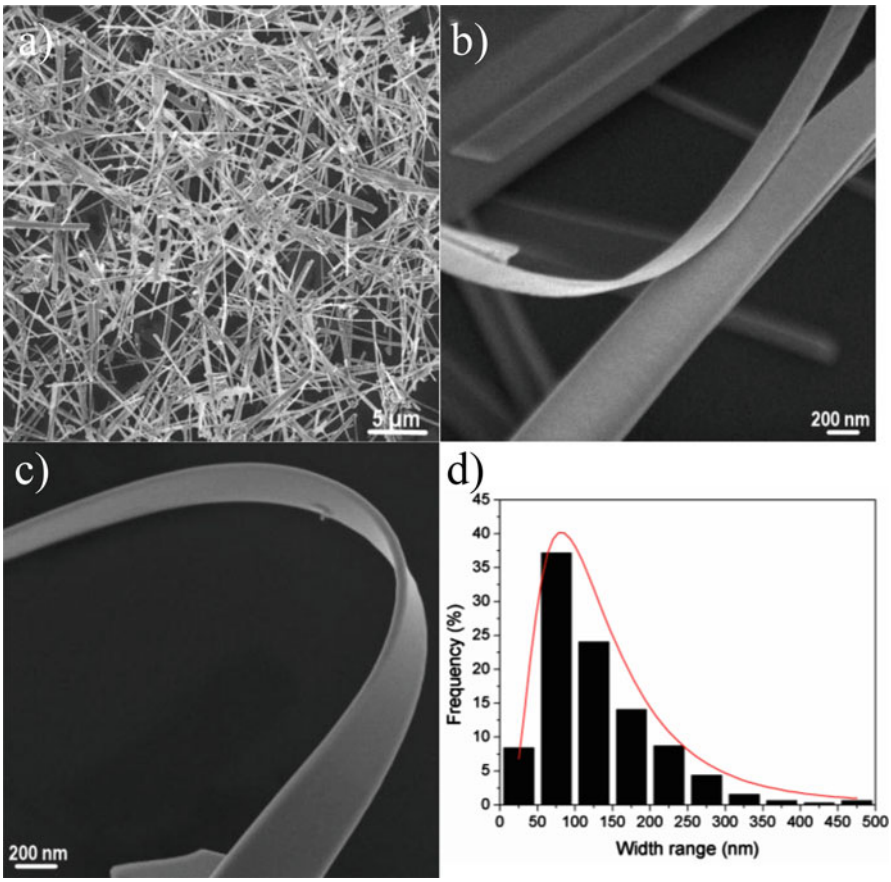

Fig. 2.3 FE-SEM images showing (**a**) a general view of the 1D SnO_2 structures and (**b**, **c**) the rectangular cross-section of the nanobelts. (**d**) Width distribution histogram of the nanobelts

surface. Figure 2.3d shows the histogram of the width distribution of the SnO_2 nanobelts presenting a single-modal width distribution with a maximum frequency between 50 and 100 nm and approximately 70% of the nanobelts smaller than 150 nm in width.

The proposed growth mechanism of SnO_2 nanobelts is the vapor-solid (VS) process [33, 38], since no metallic particles were observed at belts extremities. This process occurs due to the reduction of the SnO_2 power by the carbon black forming SnO and CO vapors inside the tube, according to the reaction showed in Eq. 2.2. The products of this reaction are transported to a lower temperature region by the N_2 gas flow and react with the O_2 inserted in the counterflow, forming the SnO_2 nanobelts and CO_2 gas (Eqs. 2.3 and 2.4).

$$SnO_{2(s)} + C_{(s)} \rightarrow SnO_{(g)} + CO_{(g)} \quad (2.2)$$

$$SnO_{(g)} + 1/2\ O_{2(g)} \rightarrow SnO_{2(s)} \quad (2.3)$$

$$CO_{(g)} + 1/2\ O_{2(g)} \rightarrow CO_{2(g)} \quad (2.4)$$

Figure 2.4 shows FE-SEM images of the SnO material grown using inert synthesis atmosphere. It was found that this material is composed of both micro-disks and nanobelts. Due to the size difference between these structures, it was possible to separate them by sedimentation. The diameter of the disks ranging from 500 nm up to several microns and their surface can be flat and smooth (Fig. 2.4a) or in steps with a sphere in the top (Fig. 2.4b), as also reported by Dai et al. and Orlandi et al. [11, 39]. Figure 2.4c indicated that the nanobelts are also flat and homogeneous along their length; most of them presenting metallic tin particles at their tips (Fig. 2.4d). The presence of these particles is related to their growth mechanism, which occurs by a self-catalytic VLS method [8, 11, 25]. It also is possible to observe from Fig. 2.4e that some SnO nanobelts present dendrites perpendicular to the growth axis of the belt. The dendrites are very thin and generally present a metallic sphere at its extremity. The width distribution histogram of the SnO nanobelts shown in Fig. 2.4f reveals the maximum width frequency to be between 20 and 30 nm and approximately 90% of the nanobelts smaller than 50 nm in width.

Since the presence of metallic spheres in one end of the SnO nanobelts was observed, it is proposed that the growth mechanism of these structures occurs by VLS [11, 25]. The VLS growth mechanism involves the presence of catalyst particles, and once they were formed during the synthesis, the SnO nanobelts grow by a self-catalytic VLS process. After the reduction of the SnO_2 power by the carbon black, only vapor of SnO and CO is formed inside the tube according to the Eq. 2.2. Since no oxygen is considered to be in the synthesis atmosphere, the SnO vapor can react with CO and produce metallic tin in the liquid phase (Eq. 2.5) and CO_2. The Sn° particles act as active sites for adsorption of SnO vapor molecules, and after they become supersaturated with SnO vapor, the first solid core of SnO is obtained. Thus, while the metallic drop remains in the liquid form and enough SnO vapor is present, the growth of the nanobelt will occur in a direction oriented by the core [11].

$$SnO_{(g)} + CO_{(g)} \rightarrow Sn^{0}{}_{(l)} + CO_{2(g)} \quad (2.5)$$

FE-SEM images of the Sn_3O_4 materials collected after the synthesis are shown in Fig. 2.5. In general, these structures present the same characteristics of the SnO_2 and SnO nanobelts, i.e., they are 1D nanostructures with dozens of micrometers in length and rectangular cross-section (Fig. 2.5a). These structures exhibit homogeneous width along the length, but a detailed characterization performed by high-resolution FE-SEM reveals that Sn_3O_4 nanobelts present a layered surface (Fig. 2.5b). The layered characteristic is related to their growth mechanisms, and it is similar to the model proposed by Ma et al. for layered SnO_2 nanobelts [40]. Figure 2.5c shows

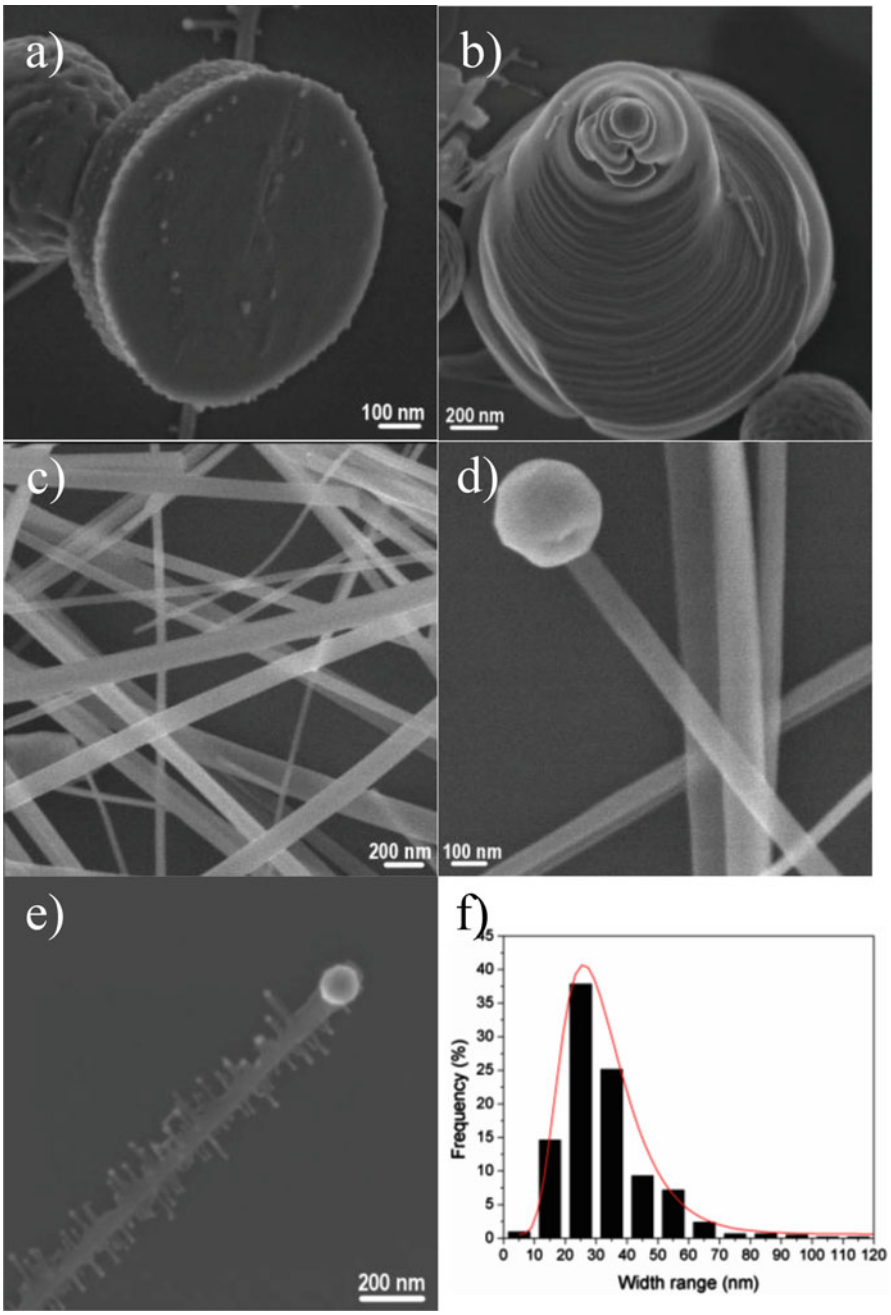

Fig. 2.4 FE-SEM images of SnO disks with (**a**) flat and (**b**) in-step surface. FE-SEM images showing (**c**) a general view of the SnO nanobelts, (**d**) their smooth surface, and (**e**) one nanobelt with dendrites in their structures. (**f**) Width distribution histogram of the belts

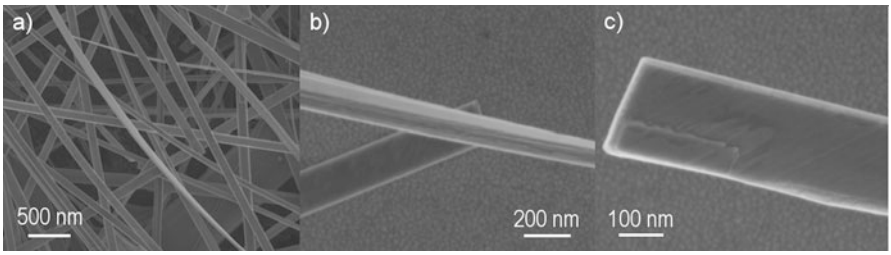

Fig. 2.5 (**a**) General view of the structures present in the Sn_3O_4 material. (**b**) High-resolution FE-SEM image showing the layered character of nanobelts. In (**c**) the initial stage of growth of a new layer on the surface of a nanobelt is showed

the initial growth stage of a new Sn_3O_4 layer. The Sn_3O_4 nanobelts present single-modal width distribution with a maximum frequency at the range of 80–120 nm.

Since no metallic particles were observed at Sn_3O_4 nanobelt extremities, it was proposed that they grow by a VS process according to Eqs. 2.2 and 2.6. After the reduction of the SnO_2 powder by the carbon black (Eq. 2.2), some SnO vapor molecules will react with the oxygen introduced in the counterflow (Eq. 2.6) in order to grow structures in an intermediate phase of tin oxide (Sn_3O_4). Despite the fact that SnO_2 and Sn_3O_4 nanobelts grow in the same synthesis, the Sn_3O_4 nanobelts are formed in a region closest to the center of the tube, i.e., in a region of lower oxygen concentration, which explains this material to grow in a more reduced state of tin oxide.

$$3SnO_{(g)} + 1/2\ O_{2(g)} \rightarrow Sn_3O_{4(s)} \tag{2.6}$$

All synthesized structures were also characterized by TEM. Figure 2.6a shows a low-magnification TEM image of SnO_2 nanobelt, confirming the homogeneous width along the length. Figure 2.6b presents the selected area electron diffraction (SAED) pattern of the nanobelt showing the single-crystalline character of each belt. The SAED pattern confirms that nanobelts grow in the SnO_2 cassiterite phase. An HRTEM image of the SnO_2 nanobelts is presented in Fig. 2.6c, and the indexed interplanar distance showed are 0.26 ± 0.01 nm and 0.33 ± 0.01 nm, which correspond to the (101) and (110) planes of the SnO_2 tetragonal structure, respectively. This means that belts grow preferentially in the [101] direction, which agrees with the XRD results.

Figure 2.7a shows a low-magnification TEM image of a flat-surface disk with an octagon shape. An HRTEM image of the disk is presented in Fig. 2.7b, and the interplanar distance indexed is 0.27 ± 0.01 nm, related to the (110) planes of the tetragonal structure of SnO (JCPDS card #6-395). The inset in Fig. 2.7b presents the SAED pattern confirming that disks are single-crystalline materials. All of the spots in the SAED pattern can be indexed by the litharge structure of SnO (tetragonal), confirming the HRTEM results. The SnO disks presented the so-called Giant Chemoresistance Response (GCR) when used as a sensor for NO_2 gas.

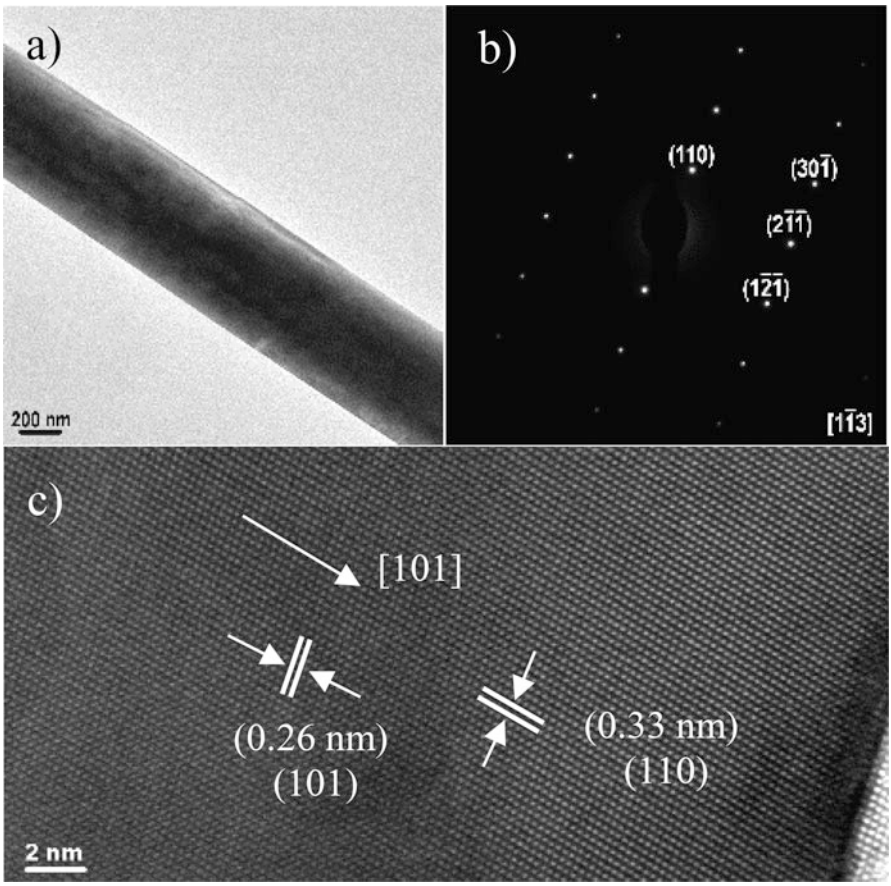

Fig. 2.6 (**a**) Low-mag TEM image of a SnO_2 nanobelt, (**b**) SAED pattern, and (**c**) HRTEM image of the belt

Figure 2.8 shows a low-magnification TEM image of typical SnO nanobelts. The corresponding EDS spectrum of the smaller nanobelt and of the nanoparticle is shown in Fig. 2.8a–c, respectively. From EDS results, it was found that the nanobelt was composed of tin oxide, while the nanoparticles consisted basically of metallic tin. Besides, the nanobelts presented a Sn concentration of 49 ± 3 (% atomic) and of 51 ± 3 (% atomic) for O, which is close to SnO stoichiometry. A SnO nanobelt with a metallic drop at one extremity is shown in Fig. 2.8d, which also presents the SAED pattern of this belt (inset). The SAED shows that the nanobelt is a single crystal and it can be indexed by the orthorhombic structure of SnO (JCPDS #13-0111). The HRTEM image of the SnO nanobelt presented in Fig. 2.8e confirms that the nanobelts are single crystalline. Additionally, the obtained interplanar distance of 0.37 nm is related to the [110] planes of the orthorhombic structure of the SnO which arises from a normal growth direction by about 8°, meaning that the SnO nanobelts grow in the [110] direction.

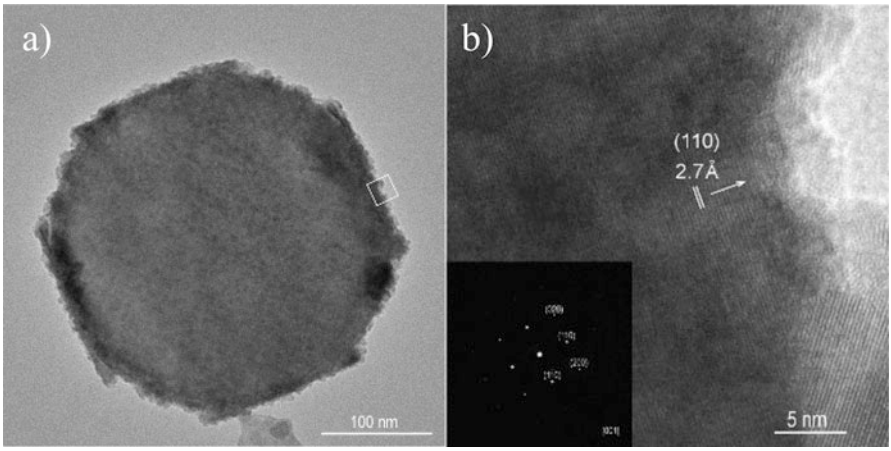

Fig. 2.7 (**a**) Low-mag TEM image of a typical faceted disk and (**b**) HRTEM image of the white square area selected in (**a**). The inset in (**b**) is the SAED pattern of the disk (Figure from Ref. [15] with permission from Elsevier)

Figure 2.9a presents a low-magnification TEM image of a Sn_3O_4 nanobelt. The color contrast is related to the mass difference along the belt, which is an evidence of the layered character of these structures (darker part of the belts represents the thicker regions). The chemical analysis performed by EDS characterization confirms that the nanobelts are composed only by Sn and O atoms, as shown in Fig. 2.9b (the carbon and copper peaks of EDS spectrum are due to the carbon-coated copper grids used in the analysis). SAED pattern (Fig. 2.9c) reveals that the nanobelts are single-crystalline structures and each layer is supposed to serve as a substrate for a layer-by-layer growth. A HRTEM image of the belt is shown in Fig. 2.9d. The indexed interplanar distance of 3.7 ± 0.1 Å is related to [−101] and [101] planes, while the 2.9 ± 0.1 Å interplanar distance is related to the [200] plane.

Tin oxide is one of the most studied materials for sensor application, so the ability to synthesize tin oxide with different oxidation states can enable in obtaining more sensitive and selective sensors. We have studied the sensor response of all tin oxide materials reported above, and results show that SnO and Sn_3O_4 materials can present better response than SnO_2. This opens new applications of nonstoichiometric tin oxide materials, and they also must be applied in other areas, such as solar cells and electronic devices.

5 Obtaining ZnO Nanostructures

The carbothermal reduction process is one of the most used methods for the growth of ZnO nanostructures with different morphologies. Along with the CVD method, it has demonstrated the possibility of obtaining a wide variety of crystal morphologies

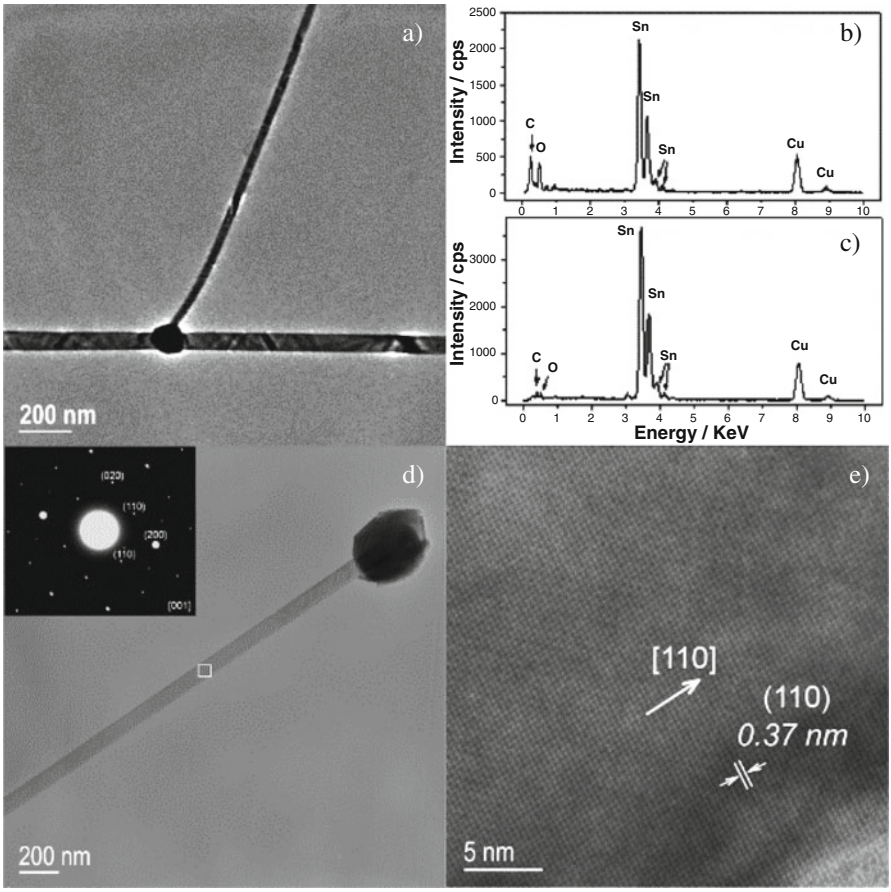

Fig. 2.8 (**a**) Low-magnification TEM image of VLS nanobelts. (**b**) EDS spectrum of the nanobelt of Fig. 2.4a. (**c**) EDS spectrum of a metallic tin nanoparticle. (**d**) Low-magnification TEM image of other VLS nanobelt. The inset shows the SAED of the belt. (**e**) HRTEM image of the SnO VLS nanobelt marked in (**d**) (Figure from Ref. [11] with permission from American Chemical Society)

with excellent properties for applications in several technological areas [41, 42]. The reduction of ZnO to Zn vapor by using carbon occurs at temperatures above 900 °C (as indicated by the Ellingham diagram), and different structures can be grown in lower temperatures with or without the presence of oxygen gas in the synthesis atmosphere. There is a great interest in the growth of ZnO nanostructures at low temperatures, since it would increase the kind of substrates for the oriented growth reducing the effects of high temperature, such as the diffusion of elements from the substrates to the nanostructures. This avoids the need for more elaborate processes including the use of buffer layer as reported by Duclère et al. [43], which used cerium oxide (CeO_2) layer to obtain epitaxial growth of ZnO thin films by pulsed laser deposition technique on sapphire substrates. The diffusion of aluminum

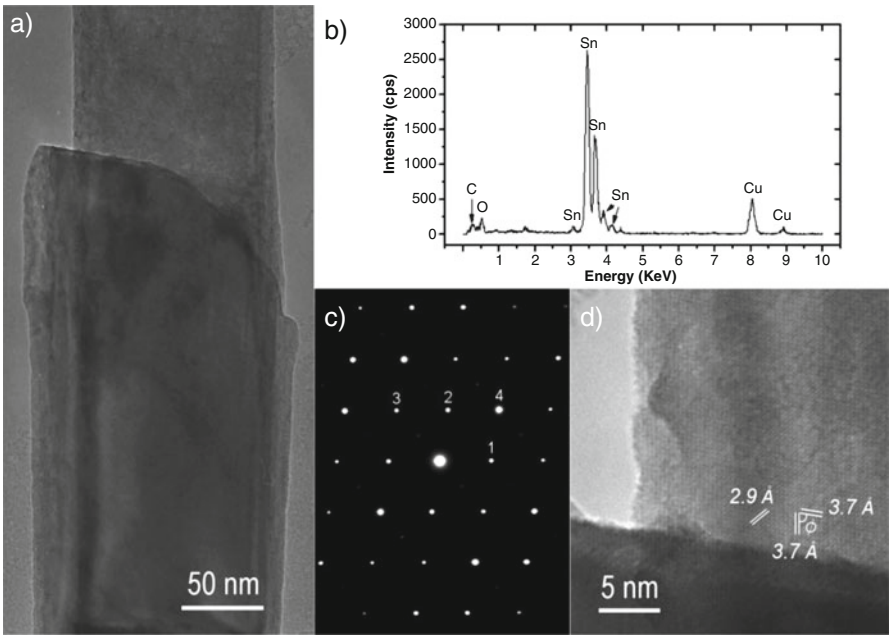

Fig. 2.9 (**a**) Bright-field TEM image of a layered nanobelt. (**b**) EDS spectrum of the thin layer of belt. (**c**) SAED pattern. The points 1, 2, 3, and 4 are related to the planes (−101), (101), (200), and (002), respectively. (**d**) HRTEM image of the belt

from the sapphire (Al_2O_3) may be unfavorable to the production of epitaxial ZnO at temperatures around 900 °C, leading to the formation of the $ZnAl_2O_4$ layer located at the interface between ZnO and sapphire [44].

Lim et al. [45] studied the formation of zinc oxide using graphite and three types of carbon black as carbon sources, whose surface areas were 3.5 m^2/g for graphite and 70, 236 and 1,440 m^2/g for carbon black materials. The study was conducted at 800 °C for 30 min under airflow. Results suggested that the reduction of ZnO to Zn vapor is strongly linked to the surface area of the carbon source, since increasing its surface area increases the formation of zinc silicate islands until complete formation of a zinc silicate layer. Finally, using the carbon black with larger surface area, ZnO nanorods were grown over zinc silicate layer (Figure 2.10). Authors associated the formation of zinc silicate, followed by the growth of ZnO nanorods, due to the increased formation of the Zn vapor phase.

Hence, the proposed mechanism of ZnO reduction is associated with (i) carbon vaporization via carbon dioxide to form carbon monoxide, (ii) the carbon monoxide diffusion for surface of ZnO, (iii) reduction of ZnO by carbon monoxide forming Zn vapor, and (iv) diffusion of Zn vapor and the carbon dioxide returning to the first stage.

The ZnO reduction kinetics in the presence of carbon can be improved by using additives such as Fe_2O_3, mills scale, and $CaCO_3$ [46]. Usually, additives are used to generate a percentage of Zn from the ZnO powder. The increased reaction rate

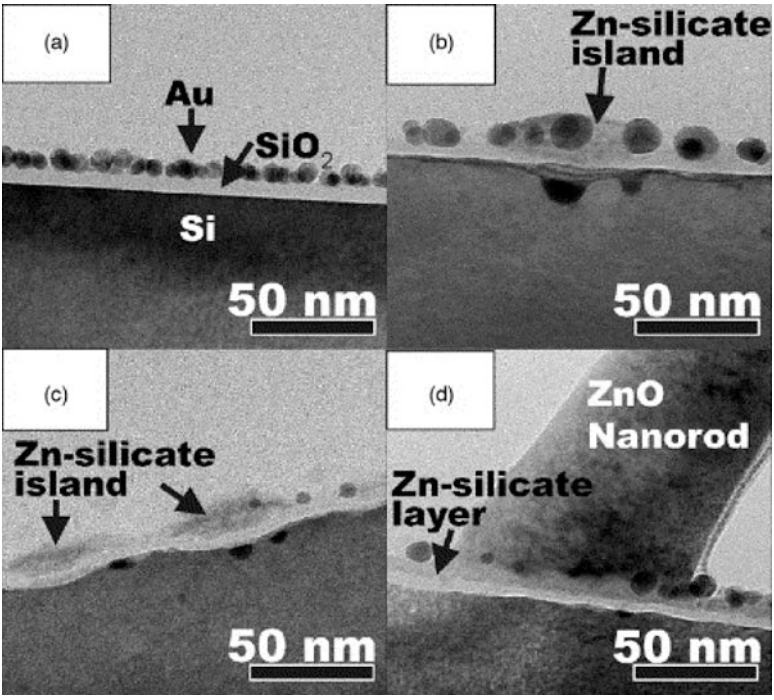

Fig. 2.10 Cross-sectional TEM micrographs of samples fabricated by using (**a**) graphite (3.5 m^2/g), (**b**) *carbon black* (70 m^2/g), (**c**) *carbon black* (236 m^2/g), and (**d**) *carbon black* (1440 m^2/g) carbon source (Figure from Ref. [45] with permission from Elsevier)

by using additives to the mixture of ZnO and carbon may be related to the easy production of CO and CO_2 gases by reaction of these additives with solid carbon, and, therefore, the Boudouard reaction is promoted on the carbon surface, which results in a rapid reduction rate. Figure 2.11 compares the reduction rate curves with various additives in certain weight percentages of ZnO at 1323 K. From this, the spherical shrinking core model (SCM) is well diffused to calculate and compare the energy response in the absence and presence of additives and has proven to be useful to describe the kinetics of the reaction.

Carbothermic reduction processes using microwave radiation has been employed in order to reduce energy costs and promote improvements in reduction rates [47, 48]. The method consists of heating a mixture of ZnO and a reducing agent rich in carbon with the incidence of microwave radiation. In the processing of ceramic materials, the energy of microwaves interacts with the matter at the molecular level, and material heating depends on the dielectric properties, the depth of penetration, as well as the frequency of microwave [49]. The dielectric properties of materials can in principle be considered as one of the most important features to evaluate the effects of heating due to microwaves, and the ability of a dielectric material to absorb microwave energy is given by its permittivity.

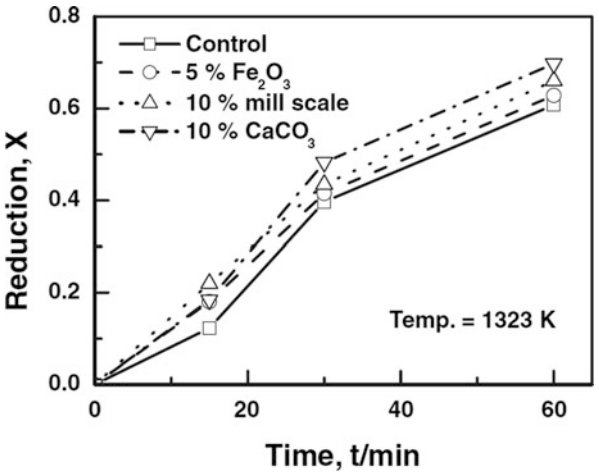

Fig. 2.11 Effect of additives on the ZnO carbon reaction system (Figure from Ref. [46] with permission from The Japan Institute of Metals)

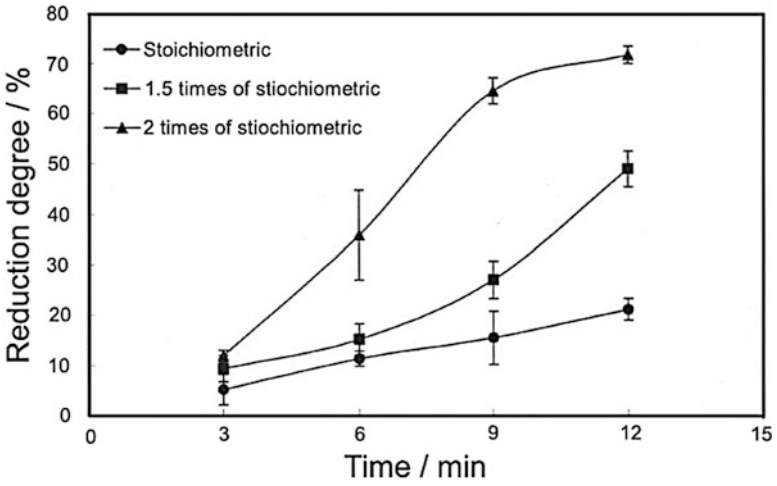

Fig. 2.12 Effect of carbon stoichiometry on microwave reduction of zinc oxide concentrate (Figure from Ref. [52] with permission from Elsevier)

Although the permittivity (and dielectric loss) of ZnO increases by increasing the temperature [50], its value is small at room temperature, resulting in a slower heating in the presence of microwaves [51]. However, carbon sources present high-microwave absorption and are the main responsible for the heating, which consequently promote the reduction of ZnO. A higher reduction rate can be achieved by increasing the carbon concentration in the mixture. Figure 2.12 shows the percentage of the ZnO reduction as function of time for different stoichiometries of ZnO and carbon source using microwave as a heating source.

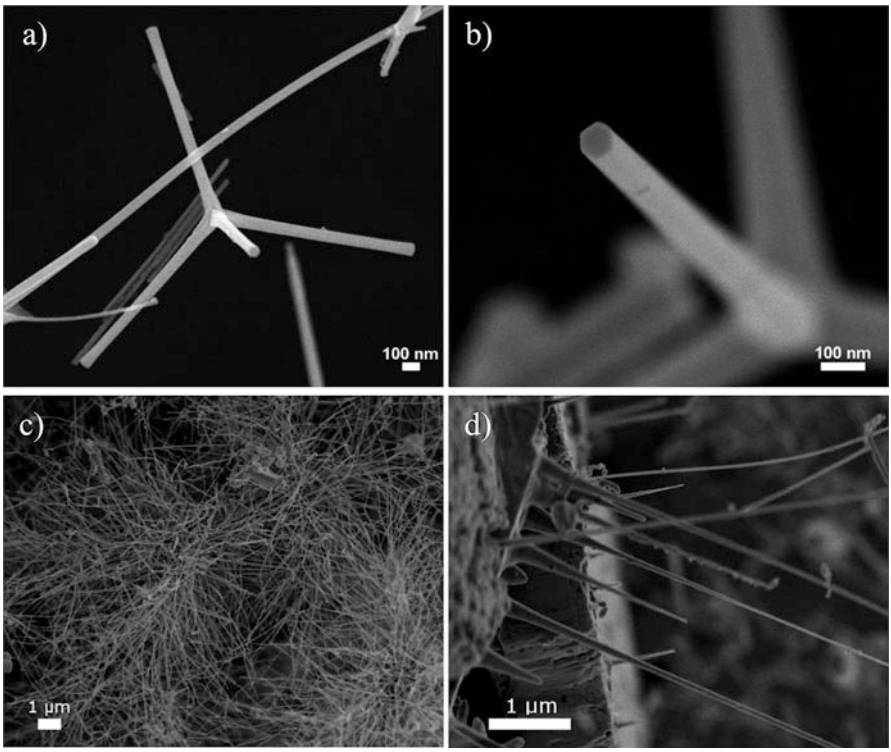

Fig. 2.13 FE-SEM images of ZnO tetrapods synthesized by the carbothermal reduction process, (**a**) an individual tetrapod, (**b**) detail of the hexagonal shape, (**c**) nanowires grown on a silicon substrate, and (**d**) growth of ZnO nanowires from plates

Using the carbothermal reduction process associated with other techniques, different ZnO nanostructured morphologies with peculiar properties can be obtained, and tetrapods and nanowires are the most common shapes.

From Fig. 2.13a–d, it is possible to observe the effectiveness of the method for obtaining tetrapods (Fig. 2.13a, b) [14] and nanowires (Fig. 2.13c, d). The carbon black was used as carbon source in the molar ratio of 1:1, and the synthesis was performed at 1,100 °C. Tetrapods have a hexagonal cross-section and a diameter lower than 100 nm. In this case, no support substrate or any types of metal catalyst were necessary to induce the growth, which is based on the VS model. For the ZnO nanowires, silicon substrates with Au catalyst layer were used to induce the growth. However, the wires grow from a layer containing ZnO plates over the silicon substrate. There is considerable homogeneity of wires with a circular cross-section, and their diameters are below 100 nm. ZnO usually crystallizes in the hexagonal wurtzite crystal structure, which is composed of Zn^{2+} and O^{2-} arranged in a tetrahedral shape and stacked alternately along the direction of the c-axis.

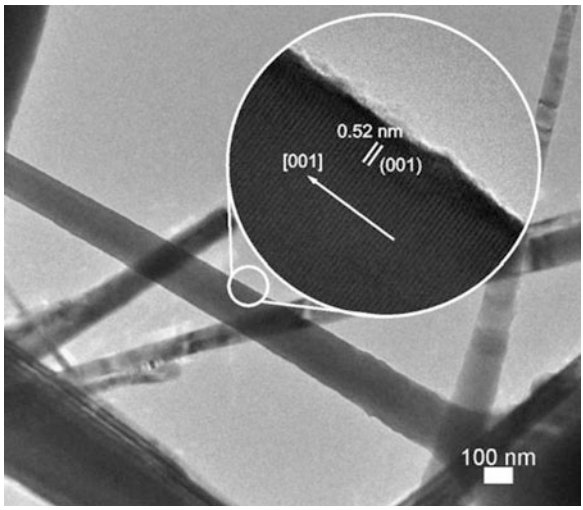

Fig. 2.14 Image of an individual ZnO tetrapod. In the inset, a HRTEM image is shown (Figure from Ref. [14] with permission from Hindawi Publishing Corporation)

Figure 2.14 shows the crystallinity degree of the tetrapods from the HRTEM image, where it is possible to confirm that material grows free of defects, featuring each "foot" of the tetrapod as a single crystal. The interplanar distance of the crystal planes in the growth direction has 0.52 nm, which refers to the (001) plane. This plane makes an angle of 90° to the growth direction of each tetrapod foot. Therefore, the [001] is the growth direction of ZnO tetrapods, which is preferred due to the self-catalytic property of the (001) plane for the ZnO structure [53].

6 Indium Tin Oxide Nanowires

Indium tin oxide (ITO) is one of the most studied transparent and conductor oxides (TCOs) used in optical electronics applications to combine high-optical transparency and high electrical conductivity [54–56]. It may be formed either by tin-doped indium oxide or vice versa, having the replacement of some indium atoms by the tin atoms. The growth of 1D ITO nanostructures has been reported by several groups since the first study on In_2O_3 nanobelts in 2001 [13, 57–59]. ITO nanowires, which have a large surface area, high electrical conductivity, and high crystallinity, can allow novel applications such as it interconnects in integrated nanoscale devices and electrodes for solar cells [58, 60, 61].

Due to the practical importance of ITO material, many methods have been used to prepare ITO nanostructures (e.g., nanowires, nanobelts, and nanorods), such as sputtering [60], coprecipitation annealing [62], electrospinning [63], pulsed laser ablation process [64], thermal evaporation [58, 59, 65], and carbothermal reduction [13, 66, 67, 68].

Among these methods, the carbothermal reduction syntheses result in the production of nanowires with features such as excellent homogeneity and crystallinity, besides allowing the obtaining of materials at lower temperatures compared to conventional thermal evaporation [13, 67].

ITO nanowires were synthesized by a carbothermal reduction method using the co-evaporation of oxides (In_2O_3 e SnO_2) mixed with carbon black as the reducing agent. As discussed above, in this process, the reaction between carbon and oxides is crucial, and thus the temperature and atmosphere during the synthesis must be tightly controlled, especially for avoiding the presence of oxygen, given that this can react with carbon before it reduces the oxides. Accordingly, several parameters may alter the composition, morphology, and yield of the grown material; the most significant parameters are the composition of the starting material (proportion of carbon/oxide) and the inert gas flux, followed by the time and temperature of synthesis.

Results obtained by changing the oxide to carbon black ratio in the starting material allowed good control of the nanowire stoichiometry enabling to obtain ITO nanowires in In_2O_3 or SnO_2 structures. Thus, properly controlling the ratio between carbon black and the oxides, the In:Sn ratio in the nanowires, and consequently the doping level, can be controlled, which is a determining factor for the conductivity of the material [68].

The influence of synthesis parameters was studied in detail for obtaining ITO nanowires, and it was found that the growth parameters which combine characteristics such as homogeneity, transparency, conductivity, and yield were the molar ratio for the starting material of $1SnO_2 + 1C$ and $1In_2O_3 + 1C$, nitrogen flow rate of 80 cm^3/min, synthesis time of 60 min, and temperature of 1150 °C. Synthesis details are given in ref. [67].

The XRD pattern (Fig. 2.15) of the collected materials can be indexed by the following phases: $In_{0.2}Sn_{0.8}$ (JCPDS card # 48-1547) and ITO (card # 89-4597). It is important to mention that it is not possible to distinguish the ITO and In_2O_3 phases without Rietveld refinement. The Al peaks are related to the aluminum sample holder used in the XRD measurements and have no correlation with the sample. The ITO phase is present in a higher amount than the metallic alloy, and have preferential orientation for the (400) planes (35.5°). No tin oxide phases were observed because following the phase diagram of In_2O_3 and SnO_2 [69], up to about 15 mol% of tin atoms can be in the solid solution in the In_2O_3 matrix without any secondary phase.

From the FE-SEM images in Fig. 2.16, it is possible to observe that ITO material is composed of 1D structures with well-defined edges, having homogeneous width along their lengths and no apparent superficial defects. Besides, we note that materials have a square cross-section due to the cubic phase of ITO, meaning ITO structures are nanowires. The metallic spheres at one extremity of wires suggest that growth mechanism of the wires follows a vapor-liquid-solid (VLS) process.

Using HRTEM characterization, it was possible to confirm that the wires grow in the (100) planes of the ITO phase (Fig. 2.17). This result agrees with the XRD analysis, which showed preferential orientation for this family of planes and also

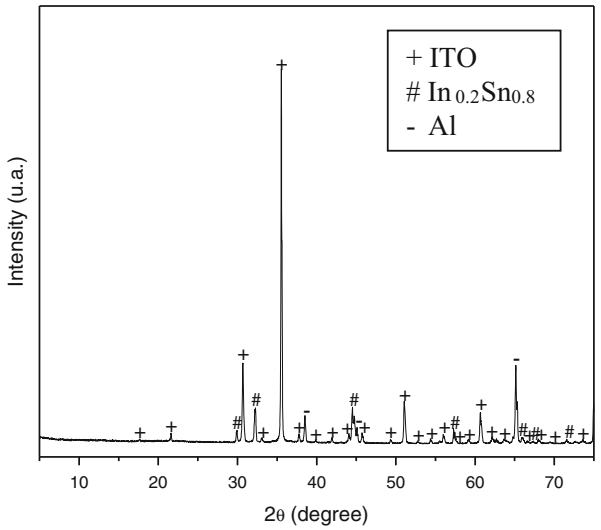

Fig. 2.15 XRD pattern of the collected material after the synthesis

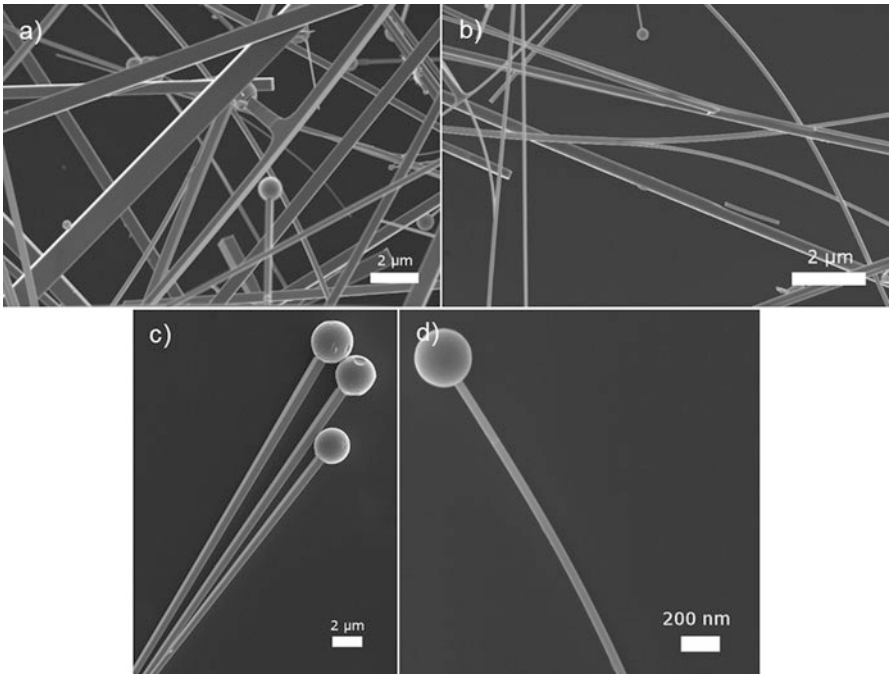

Fig. 2.16 (**a**,**b**) Low magnification FE-SEM images of typical ITO nanowires obtained at 1,150 °C. (**c**,**d**) High magnification images of ITO nanowires presenting metallic droplets at extremities

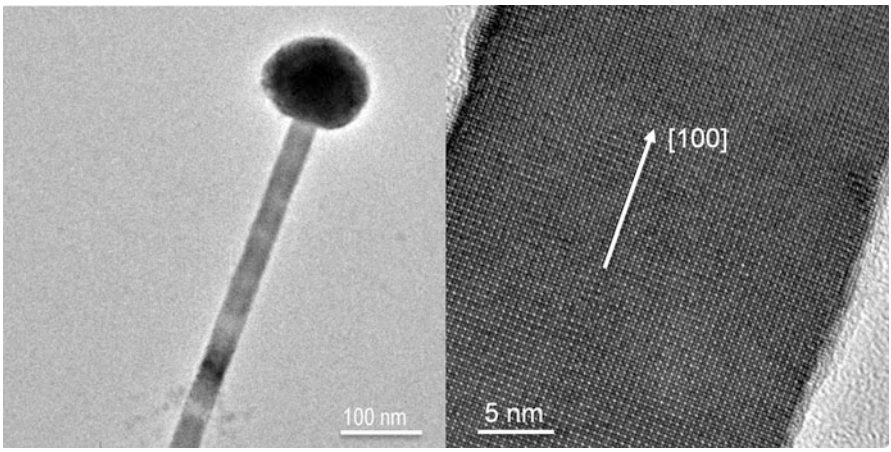

Fig. 2.17 TEM image of a typical ITO nanowire and the respective high-resolution (HRTEM) image showing the growth direction of wires

explains the origin of the square cross-section of ITO nanowires. The EDS study revealed that the wires are constituted of indium, tin, and oxygen atoms with a In:Sn proportion of 89:11 at%, confirming that carbothermal reduction is an efficient method to obtain 1D ITO nanostructures. Meanwhile, the chemical analysis showed that the spheres are composed of a Sn-rich Sn-In alloy with the same proportion obtained by XRD [67].

When obtaining ITO nanowires, the catalyst is generated in its own synthesis, meaning that the growth mechanism is related to a self-catalytic VLS process. The reactions that occur from the mixture of indium oxide with carbon during synthesis are:

$$In_2O_{3(s)} + C_{(s)} \rightarrow In_2O_{(g)} + CO_{2(g)} \tag{2.7}$$

$$In_2O_{(g)} + CO_{(g)} \rightarrow 2In^0{}_{(l)} + CO_{2(g)} \tag{2.8}$$

Then, the SnO_2 is reduced to metallic tin through the Eqs. (2.2) and (2.5). The In_2O_3 can also be reduced to metallic indium by means of the Eqs. (2.7) and (2.8) when the In_2O reacts with the carbon monoxide generated by the Eq. (2.2). These equations indicate how the catalyst metals are generated to adsorb vapor and allow growth of ITO nanowires.

It is known that these reactions occur more readily at higher temperatures, and ITO nanowires were synthesized from 1,000 to 1,200 °C. However, results indicated that at higher temperatures the carbothermal reduction process produces a significant increase of tin amount in the synthesis atmosphere. Another consequence of performing synthesis at higher temperatures is the increased width/thickness ratio of the nanowires (Fig. 2.18a). In some cases, it leaves the formation of microwires

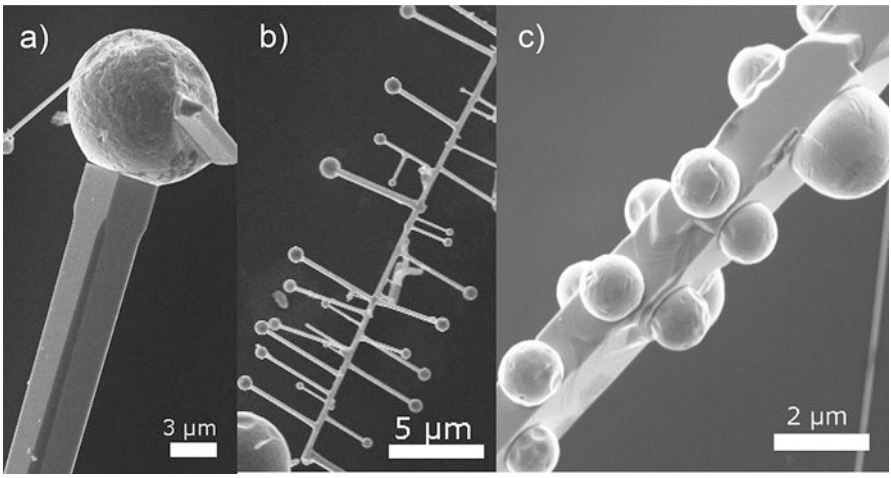

Fig. 2.18 (**a**) Detail of a ITO nanowire presenting square cross section. (**b**) A ITO nanowire with perpendicular dendrites and (**c**) initial stage of dendrite growth

(width greater than 1 μm) instead of nano-sized structures. The increase in the nanowire's width is related to the increased diameter of the catalyst metallic drop at higher temperatures. Some synthesized nanowires showed a great concentration of dendrites, which is related to the increased amount of metallic tin available in the atmosphere of synthesis (Fig. 2.18b). Figure 2.18c illustrates the deposited metallic spheres on a nanowire edge that would give rise to dendrites.

From the results shown above, it is possible to note the versatility to produce ITO nanowires by carbothermal evaporation method. Wires grow by a self-catalytic VLS process, which avoid contamination by an external catalytic agent. However, when there is a need for growing nanowires on specific sites on a substrate, it is possible to use the catalyst VLS growth (usually using gold as catalyst), which allows a more controlled growth position [65, 70].

In short, it can be concluded that the ITO nanowire's synthesis by carbothermal reduction enables, besides versatility and high performance, to control the doping level, the width/thickness ratio, and the presence of dendrites, depending on the desired application. Therefore, it is possible to choose the optimal synthesis conditions, which certainly will facilitate obtaining more complex materials with properties/characteristics desired for a wide range of technological applications.

References

1. Lu W, Lieber CM (2007) Nanoelectronics from the bottom up. Nat Mater 6(11):841–850
2. Zhang Q, Ha ST, Liu X, Sum TC, Xiong Q (2014) Room-temperature near-infrared high-Q perovskite whispering-gallery planar nanolasers. Nano Lett 14(10):5995–6001
3. Zhu H, Fu Y, Meng F, Wu X, Gong Z, Ding Q, Gustafsson MV, Trinh MT, Jin S, Zhu XY (2015) Lead halide perovskite nanowire lasers with low lasing thresholds and high quality factors. Nat Mater 14(6):636–642

4. Mao Y, Banerjee S, Wong SS (2003) Large-scale synthesis of single-crystalline perovskite nanostructures. J Am Chem Soc 125(51):15718–15719
5. Zhou W, Liu H, Boughton RI, Du G, Lin J, Wang J, Liu D (2010) One-dimensional single-crystalline Ti-O based nanostructures: properties, synthesis, modifications and applications. J Mater Chem 20(29):5993–6008
6. Yu S-H (2001) Hydrothermal/solvothermal processing of advanced ceramic materials. J Ceram Soc Jpn 109(1269):S65–S75
7. Xiao Z, Xia Y, Ren Z, Liu Z, Xu G, Chao C, Li X, Shen G, Han G (2012) Facile synthesis of single-crystalline mesoporous [small alpha]-Fe2O3 and Fe3O4 nanorods as anode materials for lithium-ion batteries. J Mater Chem 22(38):20566–20573
8. He C, Chang S, Huang X, Wang Q, Mei A, Shen PK (2015) Direct synthesis of pure single-crystalline Magneli phase Ti8O15 nanowires as conductive carbon-free materials for electrocatalysis. Nanoscale 7(7):2856–2861
9. Hu X, Tang Y, Xiao T, Jiang J, Jia Z, Li D, Li B, Luo L (2010) Rapid synthesis of single-crystalline SrSn(OH)6 nanowires and the performance of SrSnO3 nanorods used as anode materials for Li-ion battery. J Phys Chem C 114(2):947–952
10. Suman PH, Orlandi MO (2011) Influence of processing parameters on nanomaterials synthesis efficiency by a carbothermal reduction process. J Nanopart Res 13(5):2081–2088
11. Orlandi MO, Leite ER, Aguiar R, Bettini J, Longo E (2006) Growth of SnO nanobelts and dendrites by a self-catalytic VLS process. J Phys Chem B 110(13):6621–6625
12. Suman PH, Longo E, Varela JA, Orlandi MO (2014) Controlled synthesis of layered Sn3O4 nanobelts by carbothermal reduction method and their gas sensor properties. J Nanosci Nanotechnol 14(9):6662–6668
13. Orlandi MO, Aguiar R, Lanfredi AJC, Longo E, Varela JA, Leite ER (2005) Tin-doped indium oxide nanobelts grown by carbothermal reduction method. Appl Phys A 80(1):23–25
14. Silva RA, Orlandi MO (2016) Influence of synthesis route on the radiation sensing properties of ZnO nanostructures. J Nanomater 2016:9
15. Suman PH, Felix AA, Tuller HL, Varela JA, Orlandi MO (2013) Giant chemo-resistance of SnO disk-like structures. Sensors Actuators B Chem 186:103–108
16. Suman PH, Felix AA, Tuller HL, Varela JA, Orlandi MO (2015) Comparative gas sensor response of SnO2, SnO and Sn3O4 nanobelts to NO2 and potential interferents. Sensors Actuators B Chem 208:122–127
17. Zhong Y, Shaw LL, Manjarres M, Zawrah MF (2010) Synthesis of silicon carbide nanopowder using silica fume. J Am Ceram Soc 93(10):3159–3167
18. Huang B, Zheng X, Fan X, Song G, Lu M (2011) Enhanced rate performance of nano–micro structured LiFePO4/C by improved process for high-power Li-ion batteries. Electrochim Acta 56(13):4865–4868
19. Samsonov GV (1973) The oxide handbook. IFI/Plenum. Springer, New York
20. Dai ZR, Pan ZW, Wang ZL (2001) Ultra-long single crystalline nanoribbons of tin oxide. Solid State Commun 118(7):351–354
21. Dai ZR, Gole JL, Stout JD, Wang ZL (2002) Tin oxide nanowires, nanoribbons, and nanotubes. J Phys Chem B 106(6):1274–1279
22. Yang P, Lieber CM (1996) Nanorod-superconductor composites: a pathway to materials with high critical current densities. Science 273(5283):1836–1840
23. Yang P, Lieber CM (1997) Columnar defect formation in nanorod/Tl2Ba2Ca2Cu3Oz superconducting composites. Appl Phys Lett 70(23):3158–3160
24. Ya-Juan H, Jakob BW, Dang Sheng S, Guo-Qiang J, Xiang-Yun G (2006) Beaded silicon carbide nanochains via carbothermal reduction of carbonaceous silica xerogel. Nanotechnology 17(12):2870
25. Wagner RS, Ellis WC (1964) Vapor-liquid-solid mechanism of single crystal growth. Appl Phys Lett 4(5):89–90
26. Zhang Y, Wang N, Gao S, He R, Miao S, Liu J, Zhu J, Zhang X (2002) A simple method to synthesize nanowires. Chem Mater 14(8):3564–3568

27. Devan RS, Patil RA, Lin J-H, Ma Y-R (2012) One-dimensional metal-oxide nanostructures: recent evelopments in synthesis, characterization, and applications. Adv Funct Mater 22(16):3326–3370
28. Zhai T, Li L, Ma Y, Liao M, Wang X, Fang X, Yao J, Bando Y, Golberg D (2011) One-dimensional inorganic nanostructures: synthesis, field-emission and photodetection. Chem Soc Rev 40(5):2986–3004
29. Wang S, Yang J, Zhang H, Wang Y, Gao X, Wang L, Zhu Z (2015) One-pot synthesis of 3D hierarchical SnO2 nanostructures and their application for gas sensor. Sensors Actuators B Chem 207(Part A):83–89
30. Nagasawa K, Takao S, S-i N, Samjeské G, Sekizawa O, Kaneko T, Higashi K, Yamamoto T, Uruga T, Iwasawa Y (2015) Surface-regulated nano-SnO2/Pt3Co/C cathode catalysts for polymer electrolyte fuel cells fabricated by a selective electrochemical Sn deposition method. J Am Chem Soc 137(40):12856–12864
31. Yuan J, Li H, Wang Q, Zhang X, Cheng S, Yu H, Zhu X, Xie Y (2014) Facile fabrication of aligned SnO2 nanotube arrays and their field-emission property. Mater Lett 118:43–46
32. Yu S, Li L, Xu D, Dong H, Jin Y (2014) Characterization of SnO2/Cu/SnO2 multilayers for high performance transparent conducting electrodes. Thin Solid Films 562:501–505
33. Pan ZW, Dai ZR, Wang ZL (2001) Nanobelts of semiconducting oxides. Science 291(5510):1947–1949
34. Guan C, Wang X, Zhang Q, Fan Z, Zhang H, Fan HJ (2014) Highly stable and reversible lithium storage in SnO2 nanowires surface coated with a uniform hollow shell by atomic layer deposition. Nano Lett 14(8):4852–4858
35. Hu D, Han B, Deng S, Feng Z, Wang Y, Popovic J, Nuskol M, Wang Y, Djerdj I (2014) Novel mixed phase SnO2 nanorods assembled with SnO2 nanocrystals for enhancing gas-sensing performance toward isopropanol gas. J Phys Chem C 118(18):9832–9840
36. Zhang J, Guo J, Xu H, Cao B (2013) Reactive-template fabrication of porous SnO2 nanotubes and their remarkable gas-sensing performance. ACS Appl Mater Interfaces 5(16):7893–7898
37. Seko A, Togo A, Oba F, Tanaka I (2008) Structure and stability of a homologous series of tin oxides. Phys Rev Lett 100(4):045702
38. Wang X, Liu W, Yang H, Li X, Li N, Shi R, Zhao H, Yu J (2011) Low-temperature vapor–solid growth and excellent field emission performance of highly oriented SnO2 nanorod arrays. Acta Mater 59(3):1291–1299
39. Dai ZR, Pan ZW, Wang ZL (2002) Growth and structure evolution of novel tin oxide diskettes. J Am Chem Soc 124(29):8673–8680
40. Ma XL, Li Y, Zhu YL (2003) Growth mode of the SnO2 nanobelts synthesized by rapid oxidation. Chem Phys Lett 376(5–6):794–798
41. Hsu YF, Xi YY, Yip CT, Djurišić AB, Chan WK (2008) Dye-sensitized solar cells using ZnO tetrapods. J Appl Phys 103(8):083114
42. Chen W, Zhang H, Hsing IM, Yang S (2009) A new photoanode architecture of dye sensitized solar cell based on ZnO nanotetrapods with no need for calcination. Electrochem Commun 11(5):1057–1060
43. Duclère J-R, Doggett B, Henry MO, McGlynn E, Rajendra Kumar RT, Mosnier J-P, Perrin A, Guilloux-Viry M (2007) (20 − 23) ZnO thin films grown by pulsed laser deposition on CeO2-buffered r-sapphire substrate. J Appl Phys 101(1):013509
44. Gorla CR, Mayo WE, Liang S, Lu Y (2000) Structure and interface-controlled growth kinetics of ZnAl2O4 formed at the (1120)ZnO/(0112)Al2O3 interface. J Appl Phys 87(8):3736–3743
45. Lim YS, Park JW, Kim MS, Kim J (2006) Effect of carbon source on the carbothermal reduction for the fabrication of ZnO nanostructure. Appl Surf Sci 253(3):1601–1605
46. Kim B-S, Yoo J-M, Park J-T, Lee J-C (2006) A kinetic study of the carbothermic reduction of zinc oxide with various additives. Mater Trans 47(9):2421–2426
47. Fagury Neto E, Kiminami RHGA (2014) Synthesis of silicon nitride by conventional and microwave carbothermal reduction and nitridation of rice hulls. Adv Powder Technol 25(2):654–658

48. Renato de Castro E, Breda Mourão M, Jermolovicius LA, Takano C, Thomaz Senise J (2012) Carbothermal reduction of iron ore applying microwave energy. Steel Res Int 83(2):131–138
49. Chandrasekaran S, Ramanathan S, Basak T (2012) Microwave material processing—a review. AICHE J 58(2):330–363
50. L-b Z, Ma A-y, C-h L, W-w Q, J-h P, Luo Y-g, Y-g Z (2014) Dielectric properties and temperature increase characteristics of zinc oxide dust from fuming furnace. Trans Nonferrous Metals Soc China 24(12):4004–4011
51. Martin LP, Dadon D, Rosen M, Gershon D, Rybakov KI, Birman A, Calame JP, Levush B, Carmel Y, Hutcheon R (1998) Effects of anomalous permittivity on the microwave heating of zinc oxide. J Appl Phys 83(1):432–437
52. Ali Saidi KA (2005) Carbothermic reduction of zinc oxide concentrate by microwave. J Mater Sci Technol 21(05):724–728
53. Wang ZL, Kong XY, Zuo JM (2003) Induced growth of asymmetric nanocantilever arrays on polar surfaces. Phys Rev Lett 91(18):185502
54. Jiang L, Sun G, Zhou Z, Sun S, Wang Q, Yan S, Li H, Tian J, Guo J, Zhou B, Xin Q (2005) Size-controllable synthesis of monodispersed SnO2 nanoparticles and application in electrocatalysts. J Phys Chem B 109(18):8774–8778
55. Ginley DS, Bright C (2000) Transparent conducting oxides. MRS Bull 25(8):15–18
56. Wang ZL (2004) Functional oxide nanobelts: materials, properties and potential applications in nanosystems and biotechnology. Annu Rev Phys Chem 55(1):159–196
57. Chen YQ, Jiang J, Wang B, Hou JG (2004) Synthesis of tin-doped indium oxide nanowires by self-catalytic VLS growth. J Phys D Appl Phys 37(23):3319
58. Wan Q, Dattoli EN, Fung WY, Guo W, Chen Y, Pan X, Lu W (2006) High-performance transparent conducting oxide nanowires. Nano Lett 6(12):2909–2915
59. Li L, Chen S, Kim J, Xu C, Zhao Y, Ziegler KJ (2015) Controlled synthesis of tin-doped indium oxide (ITO) nanowires. J Cryst Growth 413:31–36
60. Kim H, Park H-H, Kim J (2016) Electrical and optical properties of Ni-assisted grown single crystalline and transparent indium-tin-oxide nanowires. Mater Sci Semicond Process 48:79–84
61. Meng G, Yanagida T, Nagashima K, Yoshida H, Kanai M, Klamchuen A, Zhuge F, He Y, Rahong S, Fang X, Takeda S, Kawai T (2013) Impact of preferential indium nucleation on electrical conductivity of vapor–liquid–solid grown indium–tin oxide nanowires. J Am Chem Soc 135(18):7033–7038
62. Yu D, Wang D, Yu W, Qian Y (2004) Synthesis of ITO nanowires and nanorods with corundum structure by a co-precipitation-anneal method. Mater Lett 58(1–2):84–87
63. Dandan L, Hui W, Rui Z, Wei P (2007) Preparation and electrical properties of electrospun tin-doped indium oxide nanowires. Nanotechnology 18(46):465301
64. Savu R, Joanni E (2006) Low-temperature, self-nucleated growth of indium–tin oxide nanostructures by pulsed laser deposition on amorphous substrates. Scr Mater 55(11):979–981
65. Wan Q, Wei M, Zhi D, MacManus-Driscoll JL, Blamire MG (2006) Epitaxial growth of vertically aligned and branched single-crystalline tin-doped indium oxide nanowire arrays. Adv Mater 18(2):234–238
66. Seu Yi L, Chia Ying L, Pang L, Tseung Yuen T (2005) Low temperature synthesized Sn doped indium oxide nanowires. Nanotechnology 16(4):451
67. Arlindo EPS, Lucindo JA, Bastos CMO, Emmel PD, Orlandi MO (2012) Electrical and optical properties of conductive and transparent ITO@PMMA nanocomposites. J Phys Chem C 116(23):12946–12952
68. Orlandi MO, Lanfredi AJC, Longo E (2010) Study of indium tin oxide nanomaterials obtained from vapor phase by electron microscopy. In: Mendez-Vilas A, Díaz J (eds) Microscopy: science, technology, applications and education, 4th edn, vol 3. Formatex, Badajoz, pp 1667–1673
69. Enoki H, Echigoya J, Suto H (1991) The intermediate compound in the In2O3-SnO2 system. J Mater Sci 26(15):4110–4115
70. Shen Y, Turner S, Yang P, Van Tendeloo G, Lebedev OI, Wu T (2014) Epitaxy-enabled vapor–liquid–solid growth of tin-doped indium oxide nanowires with controlled orientations. Nano Lett 14(8):4342–4351

http://www.springer.com/978-3-319-53897-6

Recent Advances in Complex Functional Materials
From Design to Application
Longo, E.; La Porta, F. de A. (Eds.)
2017, IX, 454 p. 177 illus., 112 illus. in color., Hardcover
ISBN: 978-3-319-53897-6